

Article

An Automatic Internal Wave Recognition Algorithm Based on CNN Applicable to an Ocean Data Buoy System

Guozheng Yuan ^{1,2}, Chunlin Ning ^{1,3,4,*}, Lin Liu ^{1,3,4}, Chao Li ^{1,3,4}, Yanliang Liu ^{1,3,4}, Chalermrat Sangmanee ⁵ , Xuerong Cui ², Jinkai Zhao ^{1,2}, Jiuke Wang ⁶ and Weidong Yu ⁷

- ¹ First Institute of Oceanography, Ministry of Natural Resources, Qingdao 266061, China; z21160050@s.upc.edu.cn (G.Y.); liul@fio.org.cn (L.L.); lichao@fio.org.cn (C.L.); liuyl@fio.org.cn (Y.L.); z21160008@s.upc.edu.cn (J.Z.)
- ² College of Oceanography and Space Informatics, China University of Petroleum, Qingdao 266580, China; cxr@upc.edu.cn
- ³ Key Laboratory of Marine Science and Numerical Modeling, Ministry of Natural Resources, Qingdao 266061, China
- ⁴ Shandong Key Laboratory of Marine Science and Numerical Modeling, Qingdao 266061, China
- ⁵ Phuket Marine Biological Center, Department of Marine and Coastal Resources, Phuket 83000, Thailand; csangmanee@gmail.com
- ⁶ School of Artificial Intelligence, Sun Yat-sen University, Zhuhai 519082, China; wangjk57@mail.sysu.edu.cn
- ⁷ School of Atmospheric Sciences, Sun Yat-sen University, Zhuhai 519082, China; yuwd@mail.sysu.edu.cn
- * Correspondence: cning@fio.org.cn; Tel.: +86-151-6669-6857

Abstract: The application of internal wave recognition to the buoy system is of great significance to enhance the understanding of the ocean internal wave phenomenon and provide more accurate data and information support. This article proposes an automatic internal wave recognition algorithm based on convolutional neural networks (CNN), which is used in the tight-profile intelligent buoy system. The sea profile temperature data were collected using the Bailong buoy system in the Andaman Sea in 2018. The CNN network structure is applied to feature compression of ocean temperature profile data, reducing the input feature amount of the feature recognition network, thereby reducing the overall algorithm parameters and computational complexity. By adjusting the number of convolution kernels and the length of convolution steps, the original data features in the time domain and the space domain are compressed, respectively. The experimental results show that the identification accuracy and robustness of this method are clearly superior to those of other methods. Additionally, the parameter number and calculation amount of this algorithm are very tiny, which greatly improves the possibility of its deployment in the buoy system.

Keywords: internal wave recognition; buoy system; convolutional neural networks; model optimization; feature extraction



Citation: Yuan, G.; Ning, C.; Liu, L.; Li, C.; Liu, Y.; Sangmanee, C.; Cui, X.; Zhao, J.; Wang, J.; Yu, W. An Automatic Internal Wave Recognition Algorithm Based on CNN Applicable to an Ocean Data Buoy System. *J. Mar. Sci. Eng.* **2023**, *11*, 2110.

<https://doi.org/10.3390/jmse11112110>

Academic Editor: Angelo Rubino

Received: 16 September 2023

Revised: 15 October 2023

Accepted: 25 October 2023

Published: 4 November 2023



Copyright: © 2023 by the authors. Licensee MDPI, Basel, Switzerland. This article is an open access article distributed under the terms and conditions of the Creative Commons Attribution (CC BY) license (<https://creativecommons.org/licenses/by/4.0/>).

1. Introduction

Internal waves are an ocean phenomenon with short periods and large amplitudes that can usually reach tens to hundreds of meters [1]. Internal waves have been observed in many sea areas [2–8]. Internal waves usually occur in the deep ocean and can change the thermohaline structure of seawater by affecting the vertical mixing of seawater, which is an important link in the transfer of large-scale and mesoscale motion energy [9,10]. The impact of internal waves on marine ecosystems is also important. One important impact is that on the supply of nutrients in the upper ocean [11], which is of great significance for ocean productivity and the construction of food chains. In addition, internal waves can also affect the suspension and reaccumulation of seabed sediments, as well as the distribution and transformation of biological and chemical substances in the seabed [12]. Internal waves also affect the species composition, community structure, and productivity of some marine ecosystems. Internal waves are also closely related to ocean utilization and

maritime activities. Internal waves can affect the navigation of underwater vehicles and the operation of offshore drilling platforms [13], and they may also affect the dynamic response of offshore platforms. Therefore, understanding the characteristics and distribution of internal waves and studying their impact on the ocean and the environment are of great significance for understanding the ocean, protecting the environment, and improving disaster prevention and reduction.

Tides are considered the most common driving force for the generation of internal waves in the ocean. However, there are also several other mechanisms that can promote the generation of internal waves. Among them, the mechanism by which internal waves are generated through the interaction of strong currents with underwater sandbars is well known for producing lee waves [14]. Furthermore, atmospheric disturbances, including wind fields and pressure fields, are important factors contributing to the generation of internal waves in the ocean. Previous studies have found that even a slow-moving pressure field can generate internal waves resembling a moving container, but on a much larger scale [15]. There are also studies on the internal waves induced by wind forces. Through these studies, it has been demonstrated that wind speed divergence and convergence, as well as spatiotemporal variations in wind fields, can trigger baroclinic instability [15–17]. Internal waves can be directly produced by eddies or indirectly through various phenomena associated with eddies, including drained energy, eddy–topography interaction, breaking of eddies, etc. [14]. Fu and Holt were the first to report the coexistence of internal waves and mesoscale vortices observed in SAR (Synthetic Aperture Radar) imagery, but the authors did not directly link the internal waves with the vortices [18]. Subsequently, this type of wave was observed in SAR imagery and pointed out by other researchers [19,20]. The Andaman Sea is located in the northeastern part of the Indian Ocean, between the Andaman Islands, the Malay Peninsula, the Nicobar Islands, and the island of Sumatra [21]. Tides are predominantly dominated by semi-diurnal tides [22]. The topography and water column structure of the Andaman Sea provide the basic conditions for the generation of internal solitary waves [23,24], making it a natural experimental field for studying internal solitary waves. In addition, the prevailing monsoon and frequent eddies in the Andaman Sea are also important factors contributing to the generation of internal waves.

At present, internal wave recognition methods based on satellite remote sensing images [25–29] and ocean profile data are commonly used [30–32]. The satellite remote sensing image method can be used to recognize internal waves by observing irregular light and dark fringes in images. With the rapid development of artificial intelligence, some scholars have carried out research on automatic internal wave recognition algorithms based on satellite remote sensing images. Celona S. et al. [27] used X-band radar to collect remote sensing images and a machine learning algorithm of a support vector machine (SVM) model to classify whether the images contained internal solitary waves or tidal internal waves, realizing the automatic detection and classification of internal waves. Bao S. et al. [28] used the target detection method to realize the internal wave automatic recognition method based on SAR remote sensing images. However, the observation range of satellite remote sensing images is usually large, and the satellite orbit is constantly changing, so it is impossible to observe specific areas for a long time. In addition, the observation of satellite remote sensing images is affected by natural factors such as weather and clouds [29], which will also affect the identification and observation of internal waves. and the characteristics of internal waves are easily confused with other features in remote sensing images (vortex, ship wake, wind, waves, etc.) [28].

In recent years, some scholars have performed related research on internal wave recognition based on ocean profile data. Zhang B. et al. [30], using the physical process of internal waves driving water particles to fluctuate up and down, proposed a method for calculating the amplitude of internal waves. The feasibility of this method was verified using data collected via a temperature chain installed on a moored buoy. However, this algorithm cannot automatically locate the position of internal waves and cannot be directly applied to automatically identify internal waves in the moored buoy system. Suanda S. H. et al. [31]

used a buoy equipped with a thermistor to collect offshore ocean temperature profile data for a month, and the collected temperature data were filtered via differential filtering. Then, the filtered data were compared with threshold values, and values greater than the standard threshold value were judged to be internal waves. Liu B. et al. [32] proposed a method of measuring internal waves based on a mobile temperature chain real-time monitoring system that was independently designed to perform the mobile real-time monitoring of internal waves, and the method was tested on a monitoring ship. However, through experimental verification, this study found that the recognition effect of the threshold method was not excellent: the recall was 83.33%, the precision was 89.74%, and the delay was 5.2444 min. Deploying the internal wave recognition algorithm to the ocean data buoy system can allow researchers to improve the efficiency of data processing and analysis, reduce the cost of data transmission and processing, improve the real-time performance of observation data, and flexibly respond to different observation situations. However, none of the above methods [30–32] can meet the needs of accurate and automatic identification of internal waves in ocean data buoy systems.

In recent years, the application of CNN in the field of ocean engineering has gained widespread use. Their application has revolutionized the way we tackle various challenges and tasks. With their ability to analyze large amounts of data and extract meaningful features [33,34], CNNs have been extensively applied in ocean engineering, including ocean data analysis, ocean environmental monitoring, marine robotics, and autonomous systems [35–42]. Him et al. [35] show that a statistical forecast model employing a CNN approach produces skilled ENSO forecasts for lead times of up to one and a half years. Jörges et al. [36] developed a novel two-dimensional mixed-data deep CNN for spatial SWH prediction in the nearshore area of Norderney, Germany. Chen Y. et al. [37] propose a meta-self-attention multi-scale convolution neural network (MSAMS-CNN) for the actuator fault diagnosis of AUVs. Jing Y. et al. [38] apply a CNN to construct the mapping relationship between wind data and wave data, which takes an hourglass configuration. Zhou Z. et al. [39] proposed a framework for ship speed extraction based on deep learning, taking into consideration the application of ship detection and tracking technology in hazy environments. Lu et al. [40] use the CNN-LSTM approach and utilize spatiotemporal information from the CYGNSS observations to establish an innovative model for ocean wind speed inversion.

In this paper, an automatic internal wave recognition algorithm based on CNN is proposed. This algorithm can be deployed directly on the buoy systems. By processing and analyzing the ocean profile temperature data collected using the buoy, the internal wave sign is extracted, and internal wave recognition is carried out by combining the neural network. The algorithm has the characteristics of real-time performance, high reliability, and automation and can meet the needs of internal wave recognition in intelligent buoys. In addition, considering the high energy consumption requirement of the buoy system, the algorithm can improve the feature extraction efficiency, reduce the number of parameters and calculation amount of the algorithm, and reduce the energy consumption of the buoy system by selecting a suitable number of convolution kernels and convolution interval.

2. Materials and Methods

2.1. Methods

In this paper, an internal wave recognition algorithm suitable for tight buoys is designed based on a neural network. The neural network algorithm used in the algorithm consists of two modules: a feature extraction module and a feature classification module. The algorithm first uses 1D-CNN [43,44] to extract features from input data and then uses a fully connected neural network to classify features.

2.1.1. Feature Extraction Module

CNNs can be divided into 1D-CNNs, 2D-CNNs, and 3D-CNNs according to input data types, and CNNs can extract more effective information from much more data [45].

The network structure is shown in Figure 1. The original data are a temperature sequence with 14 layers of lengths of 30, which contains 420 feature quantities. After the feature extraction network consisting of 1D-CNN, the data are transformed into a feature sequence with 5 layers of lengths of 8, which contains 40 feature quantities. Feature extraction can be achieved by enlarging the sampling step of the convolution operation and reducing the number of convolution kernels.

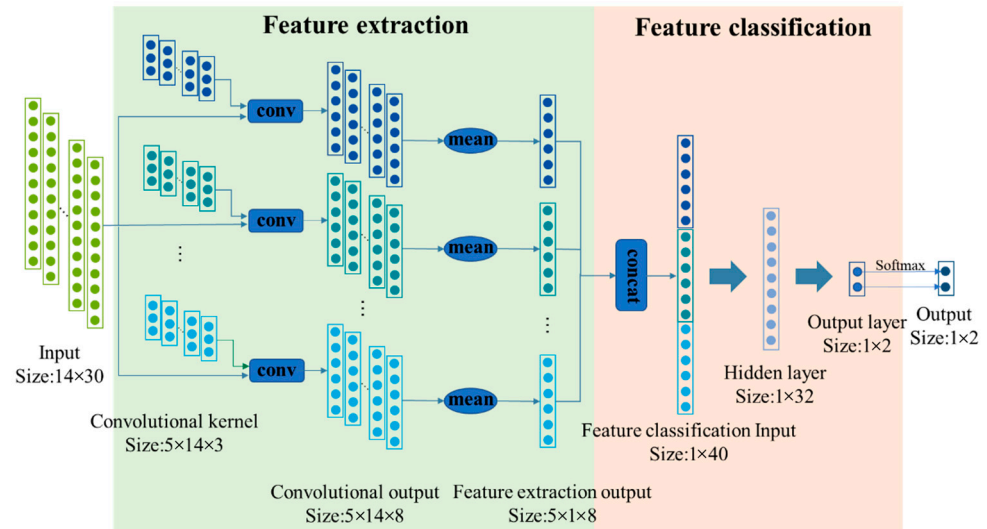


Figure 1. Internal wave recognition network structure diagram.

The correlation between adjacent moments of the ocean temperature profile data is strong, so appropriately increasing the sampling stride of the convolution operation will not affect the algorithm. The convolution kernel calculation formula for the ij -th element is shown in Formula (1).

$$ConvOutput_{ij}(n) = \sum_{m=1}^{length(w_{ij})} w_{ij}(m) \times a_j(m + n \times l) \quad n = 0, 1, 2 \dots \frac{length(a_j)}{l} \quad (1)$$

where “ a ” refers to the original data, “ $ConvOutput$ ” represents the convolution output, “ w ” is used to represent the convolution kernel, “ n ” is used to indicate the number of bits that are utilized in the convolution output, “ l ” refers to the sampling step that is used during the convolution operation, and “ $length$ ” represents the length calculation.

From Formula (1), the relationship between the input feature number “ k ”, the output feature number “ n ”, and the sampling step “ l ” of the convolution operation can be obtained as follows (As shown in Formula 2 and Figure 2):

$$n = \frac{k}{l} \quad (2)$$

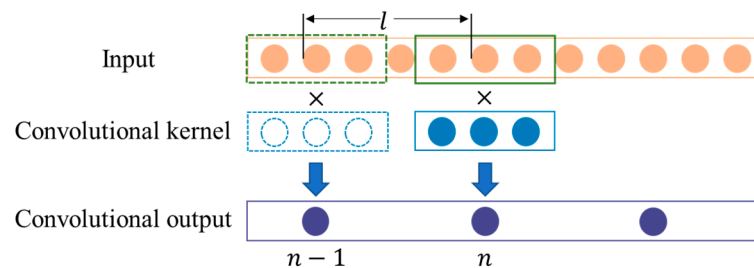


Figure 2. Convolution schematic.

This algorithm identifies internal waves through the temperature data of ocean profiles with multiple depth layers, and the temperature variation trend of adjacent depth layers is similar when internal waves arrive. To solve this problem, this method improves the efficiency of spatial features by designing a suitable number of convolution kernels. The corresponding relationship between *ConvOutput* and the original data “a” can be obtained from Formula (1), while the output of the feature extraction network is used to calculate the mean value of the convolutional output, as shown in Formula (3).

$$output_{FE} = \begin{bmatrix} \frac{1}{N} \sum_{i=1}^N ConvOutput_{i1} \\ \frac{1}{N} \sum_{i=1}^N ConvOutput_{i2} \\ \frac{1}{N} \sum_{i=1}^N ConvOutput_{i3} \\ \vdots \\ \frac{1}{N} \sum_{i=1}^N ConvOutput_{iM} \end{bmatrix} \tag{3}$$

where “*output_{FE}*” denotes the output of the feature extraction network, “N” refers to the number of layers in the raw data, and “M” represents the number of groups of convolutional kernels.

Formula (3) shows that the spatial dimension of the feature extraction output is related to the number of convolution kernel groups and has nothing to do with the spatial dimension of the original data. Therefore, this method improves the effectiveness of spatial features by testing different numbers of convolution kernel groups.

2.1.2. Feature Classification Module

The feature recognition network of this algorithm is composed of two layers of a fully connected neural network, which does not have the feature extraction capability itself but only performs a nonlinear combination of features [46]. After the output layer, a softmax layer is added to calculate the probability of a category belonging. The softmax expression used in this algorithm is shown in Formula (4).

$$output = \begin{bmatrix} \frac{e^{x_1}}{e^{x_1} + e^{x_2}} \\ \frac{e^{x_2}}{e^{x_1} + e^{x_2}} \end{bmatrix} \tag{4}$$

In the formula, *output* represents the output of the neural network, and *x₁* and *x₂* represent the two nodes of the output layer. The *output* of the classification network is a 1 × 2 matrix, where *output*(0) and *output*(1) are the probabilities of identifying no and yes internal waves, respectively.

Finally, the recognition results are shown in Formula (5).

$$y_{pre} = \begin{cases} 1 & output(1) \geq P \\ 0 & else \end{cases} \tag{5}$$

In the formula, *y_{pre}* represents the prediction result, and *P* represents the judgment probability.

2.2. Materials

2.2.1. Collect Data

The Bailong buoy [47,48] was independently integrated and developed by the First Institute of Oceanography of the Ministry of Natural Resources. The buoy device consists of a buoy body, an anchor system, a power supply unit, a meteorological sensor, a hydrological sensor, and data acquisition control and communication units, as shown in Figure 3A. Through comparison and testing with the ATLAS and TFLEX buoys of the United States, the results show that all the data for the Bailong buoy have excellent performance [49]. The temperature profile data of the Bailong buoy, placed at 9.6° N and 95.6° E in the Andaman Sea in the Indian Ocean on 14 December 2018, were used in this experiment. It

was continuously observed for 11 months and 17 days and recovered on 10 November 2019 (as shown in Figure 3B,C).

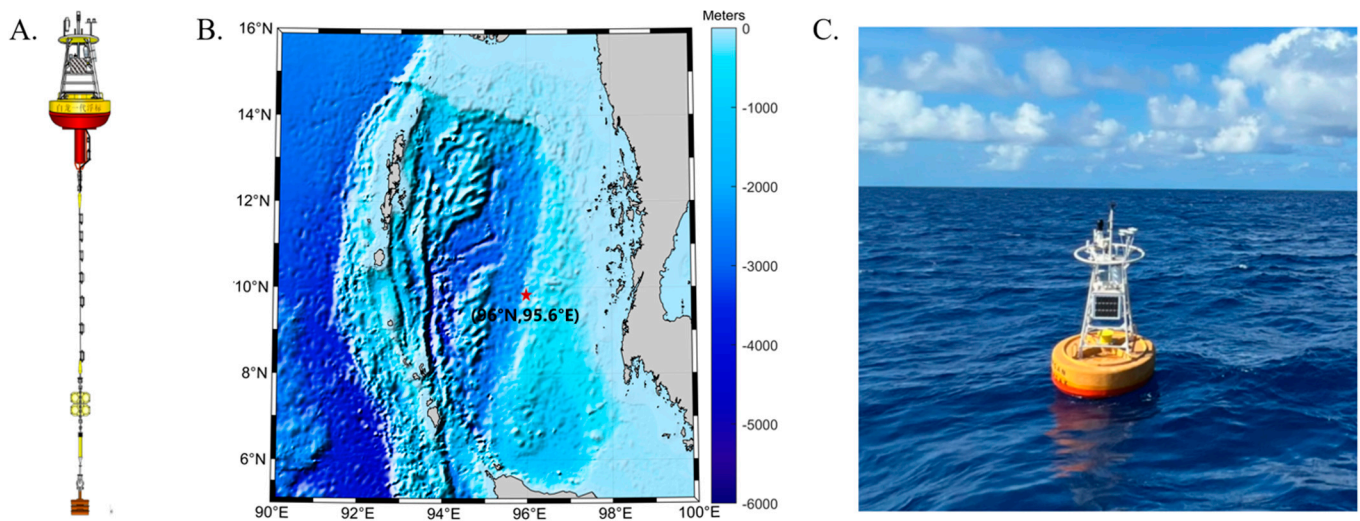


Figure 3. (A) Bailong buoy structure diagram; (B) the Bailong buoy located at 9.6° N and 95.6° E longitude in the Andaman Sea, Indian Ocean (indicated by the star in the image); and (C) the observation map of the Bailong buoy from 24 December 2018 to 10 November 2019.

A total of 18 layers of self-contained RBR sensors are installed on the buoy anchorage (the layout location is shown in Table 1). The sensor types include T, CT, and CTD. The sensor sampling frequency is set to 1 min, and the layout depth is 0–600 m, among which 0–200 m sensors are dense and 200–600 m sensors are sparse.

Table 1. RBR sensor layout position.

ID	Depth/m	Sensor Type
1	5	T
2	15	CTD
3	20	T
4	25	T
5	30	T
6	40	T
7	50	CTD
8	60	T
9	80	T
10	100	T
11	120	T
12	140	T
13	160	T
14	180	T
15	200	T
16	250	T
17	400	CTD
18	600	CTD

2.2.2. Data Annotation

The work on data standards is divided into two parts. First, the start time (T_s), extreme time (T_e), and end time (T_f) of internal waves should be annotated based on the vertical sea temperature profile diagram (as shown in Figure 4). Additionally, the amplitude (H , Formula (6)) of internal waves is determined via the variation in thermocline depth (D). In this study, the 14-degree isotherm is used as the thermocline depth. The vertical velocity component (V_p , Formula (7)) is calculated based on the amplitude and duration of the

internal waves. An internal wave is classified when the amplitude is greater than 15 m and the vertical velocity component exceeds 1 m/s [50]. In total, 1641 internal waves have been labeled.

$$H = \max\left(|D(T_e - T_s)|, |D(T_e - T_f)|\right) \tag{6}$$

$$V_p = \max\left(\frac{|D(T_e - T_s)|}{T_e - T_s}, \frac{|D(T_e - T_f)|}{T_f - T_e}\right) \tag{7}$$

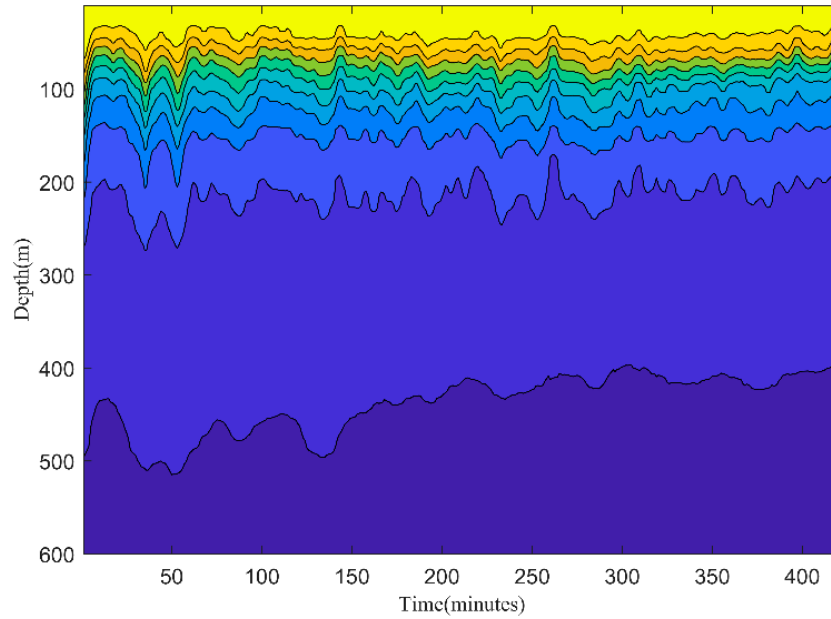


Figure 4. Vertical sea temperature profile diagram.

2.2.3. Feature Selection

According to the collected data, the ocean temperature profile is drawn. As shown in Figure 5, when the water depth is less than 200 m, the temperature changes significantly with increasing water depth, while when the water depth is greater than 200 m, the temperature does not change significantly with increasing water depth. This paper reflects the existence of internal waves through the change in the vertical distribution of water temperature. Therefore, the temperature data from 14 layers of sensors is selected as the input feature for the neural network. The sensors are positioned at depths of 15 m, 20 m, 30 m, 40 m, 50 m, 60 m, 70 m, 80 m, 100 m, 120 m, 140 m, 160 m, 180 m, 200 m, and 250 m. The selected sensor locations are mainly concentrated in the depth range of 40 m to 200 m, with the sensor coverage depth appropriately expanded.

2.2.4. Data Annotation and Splitting

The labeled dataset is divided into three parts: a training dataset, a validation dataset, and a testing dataset. The training dataset and validation dataset are used to train the neural network, and the testing dataset evaluates the performance of the final network model. The buoy collection data from 14 December 2018 to 24 January 2019 is taken as the testing dataset, and the buoy collection data from 24 January 2019 to 9 November 2019 is used as the training dataset and validation dataset. The division ratio of the training dataset and validation dataset is 8:2. The data in the dataset is added in a loop, with a new dataset being added every other minute. The specific partition of the dataset is shown in Table 2.

Table 2. Dataset partitioning results.

	Train Date Number	Val Date Number
Existential internal wave	279,782 ¹	69,945
No internal wave	37,721 ¹	9430

¹ It should be noted that the buoy cannot observe internal waves for most of the year, so there are far more data without internal waves than those with internal waves. However, in order to prevent the CNN network model from overfitting during the training process, an equal amount of data with and without internal waves is used in each round of model training.

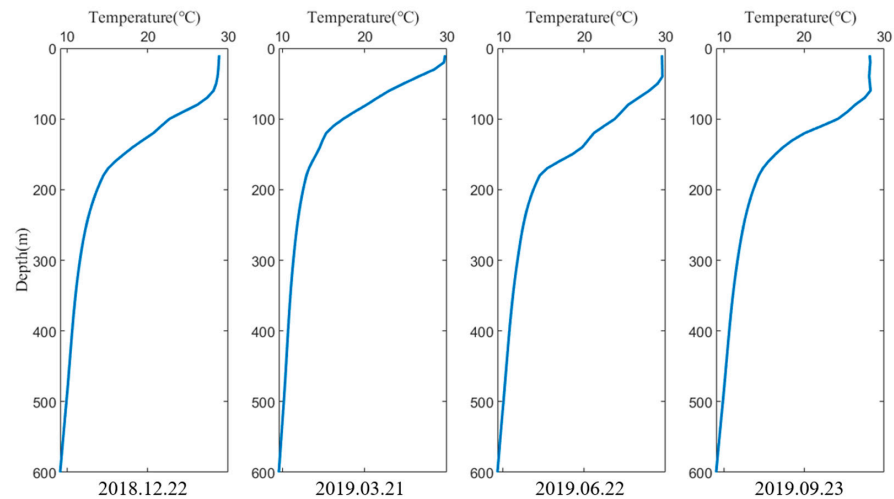


Figure 5. Diagram of temperature change in ocean profile.

2.3. Model Training

Firstly, the parameters of the feature extraction network model and feature classification network model are initialized. Secondly, for training models with a training set, the overall loss of the model is calculated through the forward propagation process, and the model parameters are updated through the back propagation process according to the loss. Finally, the validating dataset is used to evaluate the model and determine whether the model converges or not. If the model convergence proves that the training completes the derivation of the model parameters, otherwise it is proved that the model does not reach the optimal value, and it is necessary to continue to adjust the parameters until the model converges. The training process is shown in Figure 6. In the proposed model, the cross-entropy loss function [51,52] is applied, the calculation formula is shown in Formula (8), the optimizer used is Adam, and the learning rate is set to 0.001.

$$loss = -\frac{1}{2} [y_0 \log_2^{output(0)} + y_1 \log_2^{output(1)}] \tag{8}$$

In the formula, y_0 and y_1 indicate that the real label is no internal wave and there is an internal wave, respectively, and $output(0)$ and $output(1)$ are the probabilities of identifying no and yes internal waves, respectively.

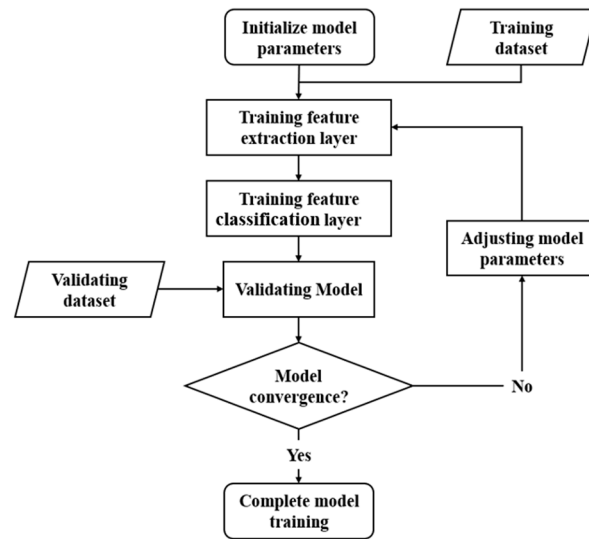


Figure 6. Model training flow chart.

3. Experimental Preparations

3.1. Experimental Evaluation

In this paper, accuracy (Formula (9)) recall (Formula (10)), precision (Formula (11)), *F1 score* (Formula (12)) [53], and delay (Formula (13)) are used as metrics of the internal wave recognition algorithm. *Accuracy* is used to measure how well the model correctly identifies internal waves. *Recall* is used to measure the model’s ability to identify internal waves. *Precision* is used to measure the accuracy of model recognition of internal waves. Generally, recall and precision are expected to both be high, but in some cases, the two indicators are contradictory. Therefore, the *F1 score* is used to reconcile recall and precision. In addition, the difference between the time when internal waves are recognized and the start time when internal waves are marked is defined as the delay. As shown in Table 3, the presence of internal waves is defined as a positive object, while the absence of internal waves is defined as a negative object.

$$Accuracy = \frac{TP + TN}{TP + FP + FN + TN} \tag{9}$$

$$Recall = \frac{TP}{TP + FN} \tag{10}$$

$$Precision = \frac{TP}{TP + FP} \tag{11}$$

$$F1\ Score = 2 * \frac{Recall * Precision}{Recall + Precision} \tag{12}$$

$$Delay = IP - SP \tag{13}$$

Table 3. Confusion matrix with or without binary classification of internal waves.

Predict Label/True Label	Existential Internal Wave	No Internal Wave
Existential internal wave	TP	FP
No internal wave	FN	TN

In the formula, *TP* indicates the number of samples that are correctly classified as having internal waves, *TN* indicates the number of samples that are correctly classified

as having no internal waves, and *FP* indicates the number of samples that are incorrectly classified as having internal waves. *FN* represents the number of samples incorrectly classified as nonexistent internal waves. *IP* represents the internal wave-identified position, and *SP* represents the internal wave-start position marked in the dataset.

In addition, to explore the effectiveness of the feature extraction network, in addition to the above evaluation indicators of the algorithm, this paper also compares the data correlation and the number of features (*N*) before and after feature extraction. Finally, to study the practicability of the algorithm, we calculate the storage cost and computing cost using different model structures, in which the storage cost is measured using the model parameter number (parameters) index and the computing cost is measured using the floating-point number (FLOPs) index.

3.2. Experimental Environment

In this study, all the experimental code source code is Python, using the PyTorch neural network architecture; the software installation version is Python 3.8.10, torch 1.11.1, and cuda11.3. The computing unit uses an RTX2080Ti graphics card with 11 GB of video memory and 40 GB of RAM.

4. Results

4.1. Algorithm Recognition Effect

To validate the good performance of the algorithm in internal wave recognition and ensure its convergence, the training and testing dataset accuracy curves for internal wave recognition were plotted in this study (Figure 7). From the graph, it can be observed that the overall recognition performance of the algorithm is quite satisfactory. The validation dataset accuracy reaches 96.84% after 100 training iterations, and the accuracy steadily converges after around 50 iterations, as seen from the overall accuracy curve.

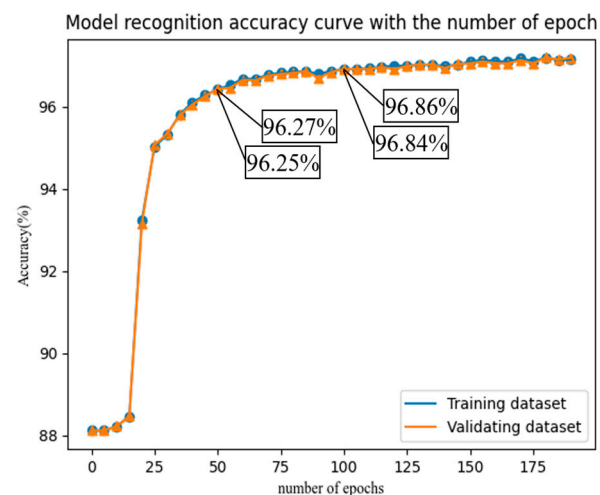


Figure 7. The convergence curve of the algorithm.

4.2. Reliability Verification

To compare the artificial intelligence method with the threshold method [19,20], the threshold method used in this study uses the same test set as the artificial intelligence method to identify internal waves. The threshold method determines the range of temperature changes within 30 min by setting a threshold (θ) to determine whether there is an internal wave. The effects of different thresholds on the experiment are shown in Table 4.

Table 4. Experimental results of the threshold method.

$\theta/^\circ\text{C}$	Recall/%	Precision/%	F1 Score/%	Delay/Minutes
2.5	100	45.49	62.53	3.1240
3	96.83	64.89	77.71	4.2696
3.5	91.27	77.18	83.64	4.8218
4	83.33	89.74	86.42	5.2444
4.5	75.40	94.06	83.70	6
5	65.87	97.65	78.67	7.0145

When the threshold recognition internal wave method is set at 2.5 °C, the recall rate is close to 100%, but the precision is close to 45.49%. As θ increases, recall decreases sharply, precision increases sharply, and delay becomes longer. When $\theta = 5$ °C, the precision is 97.65%, but the corresponding recall is only 65.87%, the delay reaches 8.2759 min. Therefore, the threshold method cannot balance the relationship between recall and precision, and the reliability of the algorithm cannot be guaranteed in practical applications.

Compared with the threshold method, the recognition effect of the artificial intelligence method has been significantly improved, as shown in Figure 8. The feature extraction network can extract and strengthen the internal wave signs and delete irrelevant features. The feature recognition network is trained to fit the internal wave sign through historical data, which takes more internal wave sign elements into consideration and has a better recognition effect than the threshold method neural network. From the experimental results, the recall rate reached 95.31%, precision was 97.53%, and the delay was reduced to 5.0862 min. Therefore, despite improving precision, the recall rate has remained at a high level, greatly enhancing the algorithm’s reliability in practical applications.

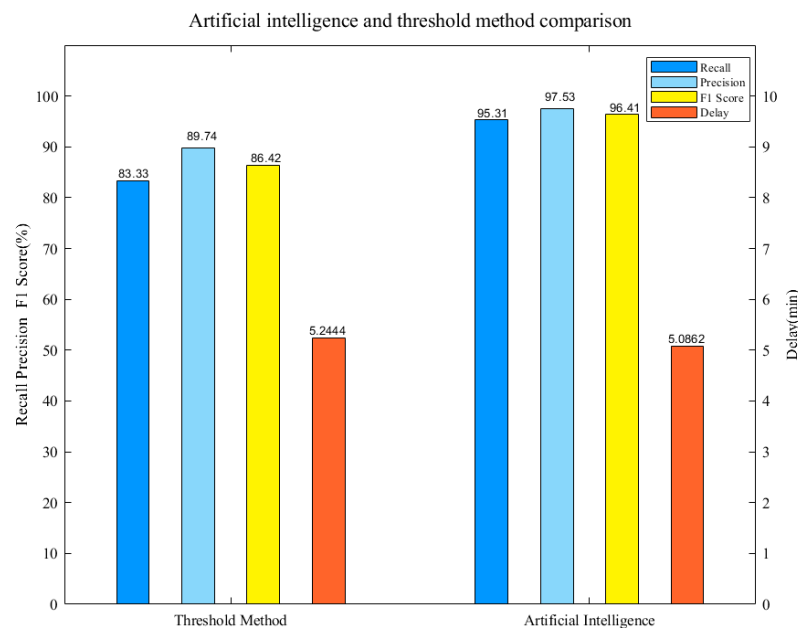


Figure 8. Comparison chart between the threshold method and artificial intelligence method (The threshold method has the best performance of the F1 score when $\theta = 3$, so the experimental results of $\theta = 3$ are selected for comparison).

To further verify the reliability of the artificial intelligence algorithm used in this paper, the artificial intelligence algorithm and threshold method are compared with the actual internal wave temperature vertical structure observation data, in which it is specified that the period when internal waves are recognized is a low state and the period when internal waves are not recognized is a high state. The comparison results are shown in Figure 9. Compared with the threshold method, the artificial intelligence method can identify more

internal waves, as shown in Figure 9A,B. Due to the slow rate of temperature change, the threshold method cannot identify these internal waves. In addition, the artificial intelligence method has fewer misidentification phenomena, as shown in Figure 9C,D. The threshold method has misidentification phenomena, which are caused by the fact that although the temperature in the misidentification period tends to rise or fall, it is not enough to define this period as an internal wave period. Artificial intelligence algorithms can improve the accuracy and reliability of internal wave recognition by extracting and identifying internal wave signs.

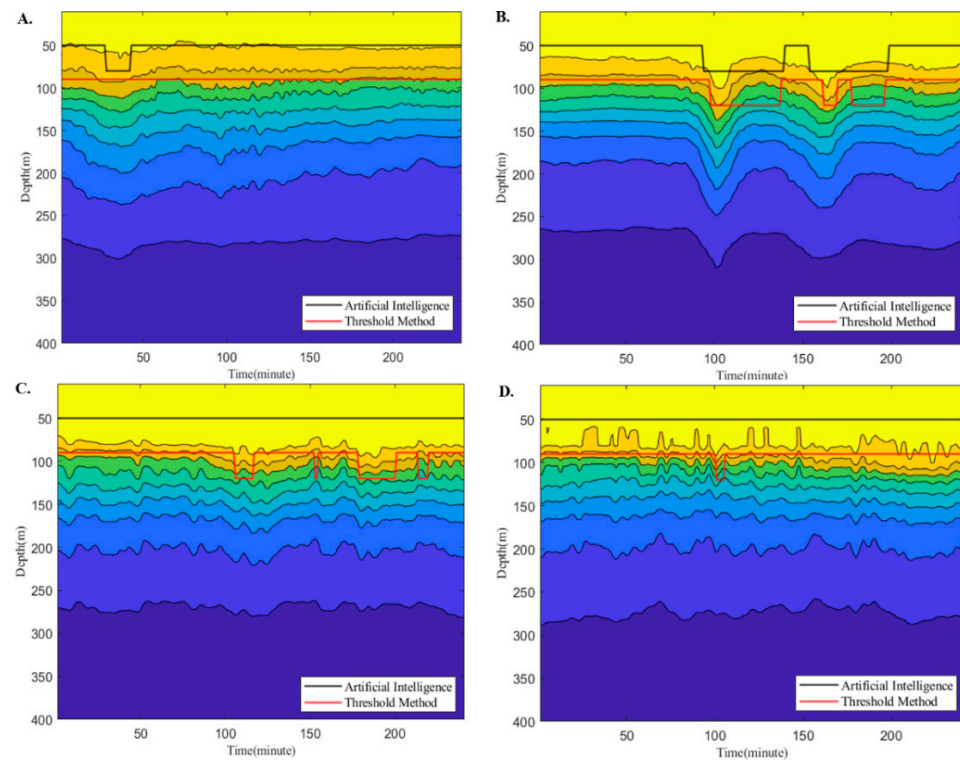


Figure 9. Threshold method and artificial intelligence method observation comparison graph. (A) Data collection was from 20:59 on 7 January 2019 to 00:59 on 8 January 2019. (B) Data collection was carried out from 18:39 to 22:39 on 22 December 2018. (C) Data collection was from 16:19 to 20:19 on 20 December 2018. (D) Data collection was conducted from 18:19 to 22:19 on 27 December 2018.

4.3. Validity Verification of the Feature Extraction Network

In this paper, by adjusting the convolution stride and the number of convolution kernels of the feature extraction network, the effectiveness of features is improved in the time dimension and space dimension, respectively. The internal wave recognition effect is best when the convolution stride is 4 and the number of convolution kernels is 5. The feature extraction network has 420 input features and 40 output features, and the efficiency of feature extraction can reach 90.48%. The correlation matrix between the input and output data of the feature extraction network is shown in Figure 10. The correlations between the original data can be reduced through the feature extraction network.

4.3.1. Sampling Step Selection of Convolution Operation

To compare the effects of sampling steps of different convolution operations on the experiment, this study compares the effects of convolution steps from 1 to 7 on the results of internal wave recognition. Figure 11 shows that when the convolution step amplitude changes from 1 to 4, the changes in recall, precision, F1 score, and delay are not obvious, but when the stride continues to increase, F1 score will have a significant downward trend, and delay will have an obvious prolongation trend because the collected underwater tem-

perature profile series is a continuously collected time series, and increasing the sampling interval by properly increasing the convolution step has little effect on the final internal wave recognition results. However, when the convolution step is raised to 5, the internal wave recognition has an obvious downward trend, so this method selects a convolution step of 4 to sample the sequence, and when the number of convolution cores is 8, the output feature number is 64, as shown in Table 5.

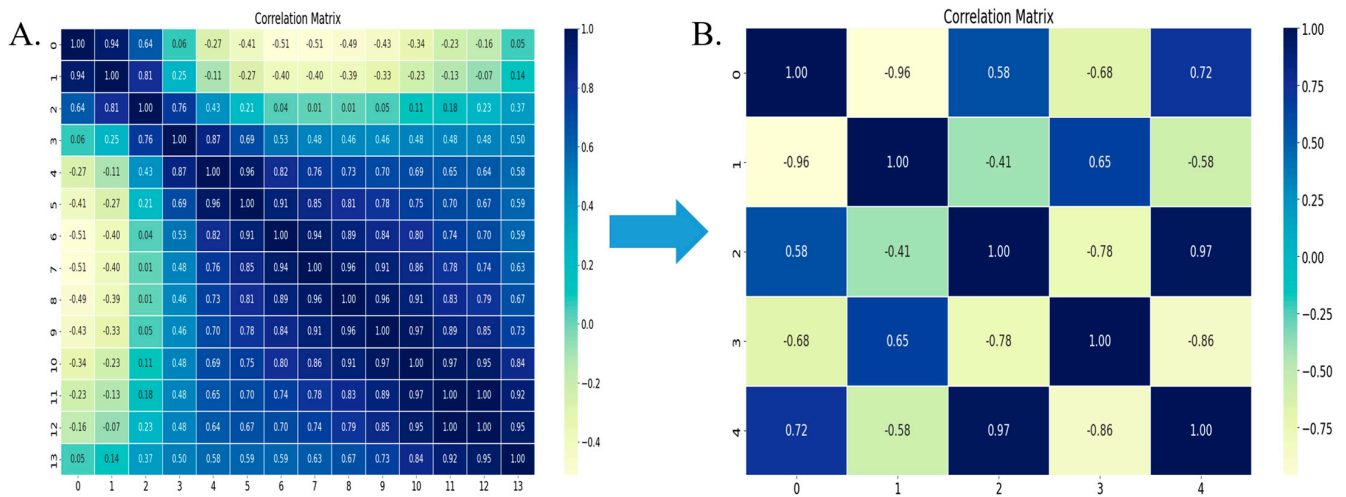


Figure 10. Comparison of the input–output correlation matrix of the feature extraction network. (A) Input feature correlation matrix. (B) Output feature correlation matrix.

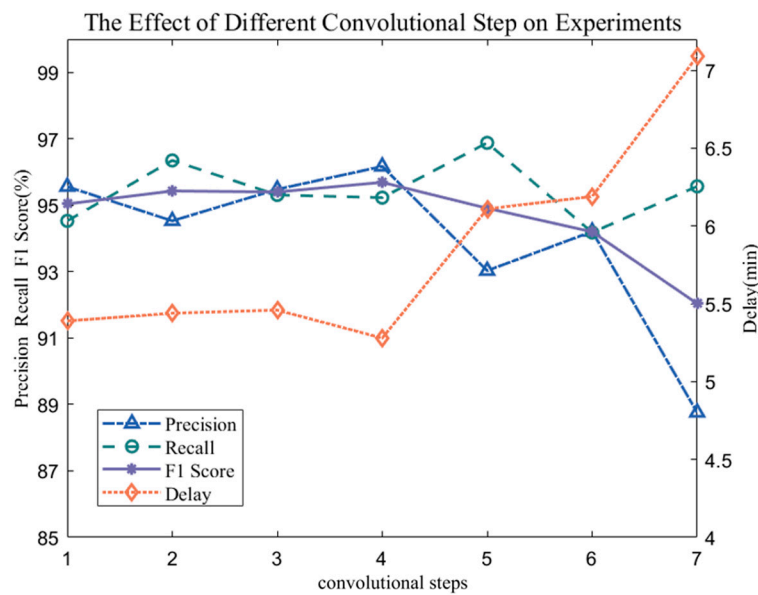


Figure 11. Influence of the convolution stride of the convolution operation on the result of internal wave recognition.

Table 5. The corresponding relationship between the convolution step and the output feature of the feature extraction network.

Convolutional Step	1	2	3	4	5	6	7
N	240	120	80	64	48	40	32

4.3.2. Selection of the Number of Convolution Kernels

To reduce the spatial information redundancy of the input data, this paper selects the appropriate number of convolution kernels to obtain more effective spatial features for internal wave recognition. The number of convolution kernels selected in the experiment is 1–9. When the number of convolution kernels is 1, it is found that the algorithm does not converge, and when the convolution kernel is 2–9, the experimental results are shown in Figure 12. When the number of convolution kernels increases from 2 to 3, the recognition effect of the algorithm is not obvious. When the number of convolution kernels is increased from 3 to 5, the recognition effect of the algorithm is significantly improved. When the number of convolution kernels is raised from 5 to 9, it is found that the internal wave recognition effect is not improved, so the final number of convolution kernels selected with this algorithm is 5, and the number of output features is 40 when the convolution step is 4, as shown in Table 6.

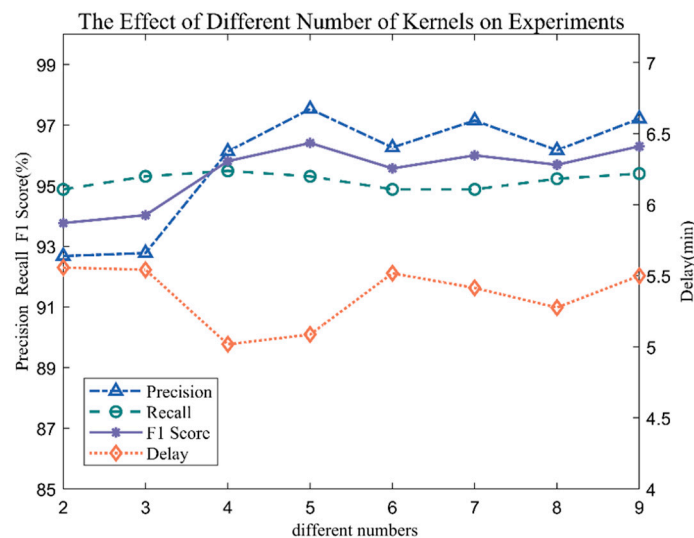


Figure 12. The influence of the number of convolution kernels on internal wave recognition.

Table 6. The corresponding relationship between the number of convolution kernels and the output features of the feature extraction network.

Convolutional Step	1	2	3	4	5	6	7
N	240	120	80	64	48	40	32

4.4. Practical Verification

By comparing the recognition results of different network structures, the one-layer convolutional neural network plus the fully connected internal wave recognition network used in this paper has the best result. Figure 13 shows the precision–recall curve of various methods, in which the precision–recall curve of this method is significantly higher than that of other network structures. As shown in Table 7, the effect of internal wave recognition is significantly improved after adding the feature extraction network, and the effect of the feature extraction network using one-dimensional convolution is also better than that of other feature extraction networks. This method has an F1 score that is 3.4% higher than the F1 score without the feature extraction network structure. The delay has been reduced by 1.22 min. Compared with the two-layer CNN and three-layer CNN feature extraction network structures, the F1 score has improved by 2.46% and 2.14%, respectively. Additionally, the delay is reduced by 0.53 min and 1.09 min, respectively. Compared with LSTM, the delay is shorter by 0.5 min, and the F1 score is increased by 2.12%.

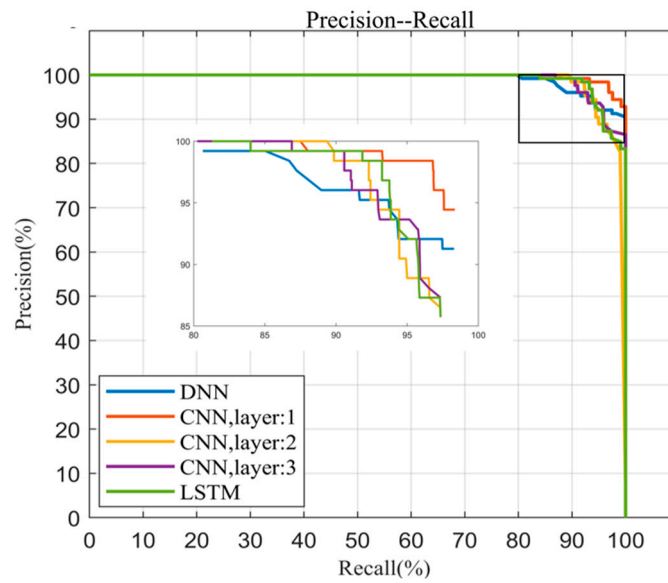


Figure 13. Precision -recall curve comparison of different networks.

Table 7. Influence of different network structures on internal wave recognition results.

	Recall (%)	Precision (%)	F1 score (%)	T (min)
DNN	0.8845	0.9829	0.9311	6.3084
CNN (layer = 1)	0.9531	0.9753	0.9641	5.0862
CNN (layer = 2)	0.9479	0.9313	0.9395	5.6154
CNN (layer = 3)	0.9627	0.9236	0.9427	5.2137
LSTM	0.9410	0.9449	0.9429	5.5893

In terms of the calculation of the number of network parameters, because this method reduces the input features of the feature recognition network by selecting the appropriate convolution steps and the number of convolution kernels, the number of parameters and computation of the algorithm are greatly reduced. As shown in Table 8, the number of parameters and the amount of calculation for this method are 1593 and 3024, respectively. Compared with the direct feature recognition method, the number of parameters is reduced by 88.2%, and the amount of calculation is reduced by 77.66%.

Table 8. Comparison of the number of parameters and computation of different networks.

	Parameters	FLOPs
DNN	13,504	13,538
CNN (layer = 1)	1593	3024
CNN (layer = 2)	9250	29,344
CNN (layer = 3)	10,034	40,864
LSTM	80,704	17,506

According to the analysis of the recognition effect of the algorithm, the number of parameters, and the amount of calculation, the algorithm has a good recognition effect, fewer parameters, and less calculation. The parameters and FLOPs of the algorithm are 1593 and 3024, respectively, so it requires very low storage capacity and computing power from the equipment. The algorithm can be directly deployed in the controller of the intelligent buoy to meet the need for automatic recognition of internal waves at the buoy end.

5. Discussion and Future Work

Internal wave detection poses several challenges and technical issues. One significant challenge is the variability and complexity of internal wave patterns, which makes their identification difficult. Additionally, the presence of noise in in situ observations further complicates the detection process. Another challenge is the lack of standardized methods for internal wave detection, leading to inconsistencies in data analysis and comparison across different studies.

Currently, some researchers have utilized deep learning methods in conjunction with satellite remote sensing images to recognize internal waves [28,54]. The basic principle involves identifying internal waves by observing the bright and dark patterns on the remote sensing images. However, due to specific conditions and time constraints, it is difficult to make continuous observations in specific areas, which limits the continuity and comprehensiveness of internal wave data. In addition, weather conditions, such as cloud cover and atmospheric interference, can also degrade image quality and affect the accuracy of internal wave identification.

In this paper, we propose several innovative methods to address the challenges of internal wave detection. On the one hand, we utilize a CNN algorithm, which takes advantage of its ability to learn complex patterns and features from field measurements. We employ advanced preprocessing techniques to improve the quality of input data and minimize noise interference. Our algorithm combines adaptive threshold and feature extraction techniques to improve the accuracy of internal wave identification.

On the other hand, we carefully select the parameters of the convolutional neural network to reduce the algorithm's parameters and computational complexity without compromising the detection performance. This allows us to deploy the algorithm in buoy systems in the future, which will help buoy systems efficiently process the redundant raw temperature profile data in any weather condition. By compressing some of the data, we can significantly reduce the computational and storage requirements without significantly affecting the detection results.

It should be noted that when applying the algorithm, certain considerations need to be considered. Fine-tuning of key parameters may be necessary to optimize the algorithm's performance for different datasets and observational conditions. It is essential to use a diverse range of training data types, including observed and modeled data and high- and low-resolution data, to ensure the algorithm's robustness and generalizability.

The potential applications of this technology extend beyond the study area to other marine regions where internal wave phenomena occur. Furthermore, the proposed method can be applied to the observation and analysis of other mesoscale atmospheric and physical oceanic phenomena, such as typhoons, eddies, and marine ecological studies. By expanding its application, this technology contributes to a better understanding of the ocean environment and its various dynamics.

In summary, this paper addresses the challenges in internal wave detection by introducing an innovative deep learning-based approach. The proposed method has the potential to be widely applied in various marine regions and opens the door to further development in the field of physical and biological oceanography.

6. Conclusions

This study presents an automated algorithm for recognizing internal waves in oceanographic buoy data based on convolutional neural networks (CNN). By exploiting the local connectivity of CNN, the algorithm effectively compresses the raw data, thereby significantly reducing the input dimension of the feature extraction network. To assess the reliability, practicality, and effectiveness of this feature extraction network, we conducted experiments using training, validation, and testing sets of Bailong buoy data. The results demonstrate the CNN-based approach's remarkable enhancement in both recall and precision of internal wave recognition, achieving a high level of performance. Moreover, we introduce an efficient feature extraction network that effectively reduces computational

complexity and the number of algorithm parameters. This research forms the groundwork for automating the dependable recognition of internal waves in intelligent buoy systems. In future work, we aim to further refine and optimize the algorithm while exploring its application in broader contexts to contribute to the advancement of oceanographic observation and early warning systems.

Author Contributions: Conceptualization, G.Y., C.N. and L.L.; Methodology, G.Y., J.W. and W.Y.; Software, G.Y.; Validation, G.Y.; Formal analysis, C.N. and C.L.; Investigation, G.Y.; Resources, C.N., Y.L. and C.S.; Data curation, Y.L., C.S. and J.Z.; Writing—original draft, G.Y., C.N., L.L. and J.Z.; Writing—review & editing, C.N., L.L., C.L. and X.C.; Visualization, G.Y.; Supervision, C.N., L.L., C.L., Y.L., X.C., J.W. and W.Y.; Project administration, C.N.; Funding acquisition, C.N. All authors have read and agreed to the published version of the manuscript.

Funding: This work was supported by the National Key Research and Development Program of China [2022YFC3104301] and financially supported by the Laoshan Laboratory [LSKJ202201601].

Institutional Review Board Statement: Not applicable.

Informed Consent Statement: Not applicable.

Data Availability Statement: Not applicable.

Acknowledgments: The authors acknowledge the funding of this study provided by the Ministry of Science (project number: 2022YFC3104301) and the Laoshan Laboratory (project number: LSKJ202201601). The authors thank Gong Xiang and Du Xing for their valuable suggestions on this study.

Conflicts of Interest: The authors declare no conflict of interest.

References

- Alford, M.H.; Peacock, T.; MacKinnon, J.A.; Nash, J.D.; Buijsman, M.C.; Centurioni, L.R.; Chao, S.Y.; Chang, M.H.; Farmer, D.M.; Fringer, O.B.; et al. The formation and fate of internal waves in the South China Sea. *Nature* **2015**, *521*, 65–69. [\[CrossRef\]](#)
- Alford, M.H.; Cronin, M.F.; Klymak, J.M. Annual cycle and depth penetration of wind-generated near-inertial internal waves at Ocean Station Papa in the northeast Pacific. *J. Phys. Oceanogr.* **2012**, *42*, 889–909. [\[CrossRef\]](#)
- Al Senafi, F.; Anis, A. Internal waves on the continental shelf of the Northwestern Arabian Gulf. *Front. Mar. Sci.* **2020**, *6*, 805. [\[CrossRef\]](#)
- Wang, J.; Xie, X.; Li, S.; Zhang, H.; Li, W. Along-slope bottom currents driven by dissipation of internal tides in the northeastern South China Sea. *Front. Mar. Sci.* **2023**, *9*, 1065824. [\[CrossRef\]](#)
- Sun, L.; Zhang, J.; Meng, J. A study of the spatial-temporal distribution and propagation characteristics of internal waves in the Andaman Sea using MODIS. *Acta Oceanol. Sin.* **2019**, *38*, 121–128. [\[CrossRef\]](#)
- Wong, S.H.; Santoro, A.E.; Nidzieko, N.J.; Hench, J.L.; Boehm, A.B. Coupled physical, chemical, and microbiological measurements suggest a connection between internal waves and surf zone water quality in the Southern California Bight. *Cont. Shelf Res.* **2012**, *34*, 64–78. [\[CrossRef\]](#)
- Da Silva, J.C.B.; Buijsman, M.C.; Magalhaes, J.M. Internal waves on the upstream side of a large sill of the Mascarene Ridge: A comprehensive view of their generation mechanisms and evolution. *Deep Sea Res. Part I Oceanogr. Res. Pap.* **2015**, *99*, 87–104. [\[CrossRef\]](#)
- Qiu, B.; Nakano, T.; Chen, S.; Klein, P. Submesoscale transition from geostrophic flows to internal waves in the northwestern Pacific upper ocean. *Nat. Commun.* **2017**, *8*, 14055. [\[CrossRef\]](#)
- Wijesekera, H.W.; Teague, W.J.; Jarosz, E.; Wang, D.W.; Fernando, H.J.S.; Hallock, Z.R. Internal tidal currents and solitons in the southern Bay of Bengal. *Deep Sea Res. Part II Top. Stud. Oceanogr.* **2019**, *168*, 104587. [\[CrossRef\]](#)
- Jensen, T.G.; Magalhaes, J.; Wijesekera, H.W.; Buijsman, M.; Helber, R.; Richman, J. Numerical modelling of tidally generated internal wave radiation from the Andaman Sea into the Bay of Bengal. *Deep Sea Res. Part II Top. Stud. Oceanogr.* **2020**, *172*, 104710. [\[CrossRef\]](#)
- Nishino, S.; Kawaguchi, Y.; Inoue, J.; Hirawake, T.; Fujiwara, A.; Futsuki, R.; Onodera, J.; Aoyama, M. Nutrient supply and biological response to wind-induced mixing, inertial motion, internal waves, and currents in the northern Chukchi Sea. *J. Geophys. Res. Ocean.* **2015**, *120*, 1975–1992. [\[CrossRef\]](#)
- Diamessis, P.J.; Jacobs, G.B. *Near-Bottom Turbulence and Sediment Resuspension Induced by Nonlinear Internal Waves*; Cornell University: Ithaca, NY, USA, 2015.
- Moore, S.E.; Lien, R.C. Pilot whales follow internal solitary waves in the South China Sea. *Mar. Mammal Sci.* **2007**, *23*, 193–196. [\[CrossRef\]](#)

14. Koohestani, K.; Stepanyants, Y.; Allahdadi, M.N. Analysis of Internal Solitary Waves in the Gulf of Oman and Sources Responsible for Their Generation. *Water* **2023**, *15*, 746. [[CrossRef](#)]
15. Morozov, E.G. *Oceanic Internal Tides: Observations, Analysis and Modeling; A Global View*; Springer: Cham, Switzerland, 2018. [[CrossRef](#)]
16. Benilov, A.Y.; Solntseva, N.I.; Filyushkin, B.N. Relationship between the variability of the wind field and internal waves. *Oceanology* **1978**, *18*, 257–266.
17. LeBlond, P.H.; Mysak, L.A. *Waves in the Ocean*; Elsevier Oceanography Series; Elsevier: Amsterdam, The Netherlands, 1978; Volume 20.
18. Fu, L.L.; Holt, B. Some examples of detection of oceanic mesoscale eddies by the SEASAT synthetic-aperture radar. *J. Geophys. Res. Ocean.* **1983**, *88*, 1844–1852. [[CrossRef](#)]
19. Joyce, T.M.; Stalcup, M.C. An upper ocean current jet and internal waves in a Gulf Stream warm core ring. *J. Geophys. Res. Ocean.* **1984**, *89*, 1997–2003. [[CrossRef](#)]
20. Lyzenga, D.; Wackerman, C. Detection and classification of ocean eddies using ERS-1 and aircraft SAR images. *Variations* **1997**, *414*, 1267.
21. Xu, M.G.; Xie, Z.H.; He, Z.R.; Liu, A.G.; Yang, J.S. Nonlinear internal waves in the Andaman Sea. *J. Photogramm. Remote Sens.* **2014**, *18*, 161–173. [[CrossRef](#)]
22. Hyder, P.; Jeans, D.R.G.; Cauquil, E.; Nerzic, R. Observations and predictability of internal solitons in the northern Andaman Sea. *Appl. Ocean Res.* **2005**, *27*, 1–11. [[CrossRef](#)]
23. Zhou, L. *Analysis of Internal Waves in the Andaman Sea and Its Adjacent Waters Based on Remote Sensing Images*; Zhejiang University: Hangzhou, China, 2018.
24. Gao, G.; Liu, C.; Zhu, C.; Jiang, C.; Wang, X. Analysis of single-ridge topography impact on internal waves' generation and propagation. *J. Trop. Oceanogr.* **2015**, *34*, 23–29. [[CrossRef](#)]
25. Zhang, X.; Wang, H.; Wang, S.; Liu, Y.; Yu, W.; Wang, J.; Xu, Q.; Li, X. Oceanic internal wave amplitude retrieval from satellite images based on a data-driven transfer learning model. *Remote Sens. Environ.* **2022**, *272*, 112940. [[CrossRef](#)]
26. Zhang, X.; Li, X. Satellite data-driven and knowledge-informed machine learning model for estimating global internal solitary wave speed. *Remote Sens. Environ.* **2022**, *283*, 113328. [[CrossRef](#)]
27. Celona, S.; Merrifield, S.T.; de Paolo, T.; Kaslan, N.; Cook, T.; Terrill, E.J.; Colosi, J.A. Automated detection, classification, and tracking of internal wave signatures using X-band radar in the inner shelf. *J. Atmos. Ocean. Technol.* **2021**, *38*, 789–803. [[CrossRef](#)]
28. Bao, S.; Meng, J.; Sun, L.; Liu, Y. Detection of ocean internal waves based on Faster R-CNN in SAR images. *J. Oceanol. Limnol.* **2020**, *38*, 55–63. [[CrossRef](#)]
29. Shen, H.; Li, X.; Cheng, Q.; Zeng, C.; Yang, G.; Li, H.; Zhang, L. Missing information reconstruction of remote sensing data: A technical review. *IEEE Geosci. Remote Sens. Mag.* **2015**, *3*, 61–85. [[CrossRef](#)]
30. Zhang, B.; Chen, W.; Chen, B.; Wang, D. Observation of the amplitude of internal waves in the South China Sea using the temperature chain. *J. Ocean Univ. China (Nat. Sci. Ed.)* **2014**, *44*, 24–28. [[CrossRef](#)]
31. Suanda, S.H.; Barth, J.A.; Holman, R.A.; Stanley, J. Shore-based video observations of nonlinear internal waves across the inner shelf. *J. Atmos. Ocean. Technol.* **2014**, *31*, 714–728. [[CrossRef](#)]
32. Liu, B. Research on measurement method of internal wave based on mobile temperature chain real-time monitoring system. *Wirel. Internet Technol.* **2022**, *19*, 6.
33. Hassanpour, M.; Malek, H. Learning document image features with SqueezeNet convolutional neural network. *Int. J. Eng.* **2020**, *33*, 1201–1207. [[CrossRef](#)]
34. Ko, Y.F.; Ju, J.W.W. Effective Elastic Properties of 3-Phase Particle Reinforced Composites with Randomly Dispersed Elastic Spherical Particles of Different Sizes. *CMES-Comput. Model. Eng. Sci.* **2021**, *129*, 1305–1328. [[CrossRef](#)]
35. Ham, Y.G.; Kim, J.H.; Luo, J.J. Deep learning for multi-year ENSO forecasts. *Nature* **2019**, *573*, 568–572. [[CrossRef](#)]
36. Jörges, C.; Berkenbrink, C.; Gottschalk, H.; Stumpe, B. Spatial Ocean wave height prediction with CNN mixed-data deep neural networks using random field simulated bathymetry. *Ocean Eng.* **2023**, *271*, 113699. [[CrossRef](#)]
37. Chen, Y.; Wang, Y.; Yu, Y.; Wang, J.; Gao, J. A Fault Diagnosis Method for the Autonomous Underwater Vehicle via Meta-Self-Attention Multi-Scale CNN. *J. Mar. Sci. Eng.* **2023**, *11*, 1121. [[CrossRef](#)]
38. Jing, Y.; Zhang, L.; Hao, W.; Huang, L. Numerical study of a CNN-based model for regional wave prediction. *Ocean Eng.* **2022**, *255*, 111400. [[CrossRef](#)]
39. Zhou, Z.; Zhao, J.; Chen, X.; Chen, Y. A Ship Tracking and Speed Extraction Framework in Hazy Weather Based on Deep Learning. *J. Mar. Sci. Eng.* **2023**, *11*, 1353. [[CrossRef](#)]
40. Lu, C.; Wang, Z.; Wu, Z.; Zheng, Y.; Liu, Y. Global Ocean wind speed retrieval from GNSS reflectometry using CNN-LSTM network. *IEEE Trans. Geosci. Remote Sens.* **2023**, *61*, 1–12. [[CrossRef](#)]
41. Bao, X.; Fan, T.; Shi, C.; Yang, G. One-dimensional convolutional neural network for damage detection of jacket-type offshore platforms. *Ocean Eng.* **2021**, *219*, 108293. [[CrossRef](#)]
42. Thongniran, N.; Jitkajornwanich, K.; Lawawirojwong, S.; Srestasathiern, P.; Vateekul, P. Combining attentional CNN and GRU networks for ocean current prediction based on HF radar observations. In Proceedings of the 2019 8th International Conference on Computing and Pattern Recognition, Beijing, China, 23–25 October 2019; pp. 440–446. [[CrossRef](#)]

43. Wu, H.; Chen, J.; Liu, X.; Xiao, Y.; Wang, M.; Zheng, Y.; Rao, Y. One-dimensional CNN-based intelligent recognition of vibrations in pipeline monitoring with DAS. *J. Light. Technol.* **2019**, *37*, 4359–4366. [[CrossRef](#)]
44. León, A.A.S.; Alvarez, J.R.N. 1D convolutional neural network for detecting ventricular heartbeats. *IEEE Lat. Am. Trans.* **2019**, *17*, 1970–1977. [[CrossRef](#)]
45. Raj, S.; Prakasam, P.; Gupta, S. Multilayered convolutional neural network-based auto-CODEC for audio signal denoising using mel-frequency cepstral coefficients. *Neural Comput. Appl.* **2021**, *33*, 10199–10209. [[CrossRef](#)]
46. Guo, M.; Li, W.; Yang, Q.; Zhao, X. Application of deep convolutional neural network in shaft trajectory recognition of sliding bearing rotor. *Vib. Shock* **2021**, *40*, 233–239. [[CrossRef](#)]
47. Lu, X.; Chen, M.; Wang, X.; Zhou, Y. Development history of marine hydrological survey equipment in China. *Ocean Devel-Opment Manag.* **2020**, *37*, 44–48. [[CrossRef](#)]
48. Ning, C.; Xue, L.; Jiang, L. The solution of global communication system sharing of Bailong buoy data. *J. Hehai Univ. (Philos. Soc. Sci. Ed.)* **2022**, *50*, 91–95. [[CrossRef](#)]
49. Freitag, H.P.; Ning, C.; Berk, P. *Atlas, T-flex, Bailong METEOROLOGICAL Sensor Comparison Test Report*; PMEL-148; NOAA Technical Memorandum OAR: Woods Hole, MA, USA, 2016.
50. Gerkema, T. An introduction to internal waves. *Lect. Notes R. NIOZ Texel* **2008**, *207*, 207.
51. De Boer, P.T.; Kroese, D.P.; Mannor, S.; Rubinstein, R.Y. A tutorial on the cross-entropy method. *Ann. Oper. Res.* **2005**, *134*, 19–67. [[CrossRef](#)]
52. Aarts, E.; Korst, J. *Simulated Annealing and Boltzmann Machines: A Stochastic Approach to Combinatorial Optimization and Neural Computing*; John Wiley & Sons, Inc.: Hoboken, NJ, USA, 1989. [[CrossRef](#)]
53. Goutte, C.; Gaussier, E. A Probabilistic Interpretation of Precision, Recall and F-Score, with Implication for Evaluation. In *European Conference on Information Retrieval*; Springer: Berlin/Heidelberg, Germany, 2005; pp. 345–359. [[CrossRef](#)]
54. Ma, Y.; Meng, J.; Sun, L.; Ren, P. Oceanic Internal Wave Signature Extraction in the Sulu Sea by a Pixel Attention U-Net: PAU-Net. *IEEE Geosci. Remote Sens. Lett.* **2022**, *20*, 1–5. [[CrossRef](#)]

Disclaimer/Publisher’s Note: The statements, opinions and data contained in all publications are solely those of the individual author(s) and contributor(s) and not of MDPI and/or the editor(s). MDPI and/or the editor(s) disclaim responsibility for any injury to people or property resulting from any ideas, methods, instructions or products referred to in the content.